

<https://doi.org/10.1038/s43247-024-01905-7>

Ophiolites in the Central Asian Orogenic Belt record Cambrian subduction initiation processes

Check for updates

Mingshuai Zhu ^{1,2}✉, Daniel Pastor-Galán ^{3,4}, Matthijs A. Smit ^{5,6}, Laicheng Miao ^{1,2}, Miao Dong ⁷✉, Fuqin Zhang^{1,2}, Dorjochoo Sanchir^{1,2}, Ariuntsetseg Ganbat⁸, Chenghao Liu^{1,2}, Ye Luo^{1,2} & Shun Li ⁹✉

Subduction initiation remains elusive because no present example exists. Ophiolites formed over nascent subduction zones in the past provide the key to constraining the processes of subduction initiation. Here we document three Cambrian ophiolites with supra-subduction zone affinity, which likely reflect the inception of a plate-boundary scale subduction zone within the Paleo-Asian Ocean. Our findings, together with a compilation of Cambrian ophiolites in the Central Asian Orogenic Belt, indicate diachronous subduction initiation(s) along a > 6000 kilometer zone within the Paleo-Asian Ocean between 536 and 528 million years ago. The subduction initiation of the Paleo-Asian Ocean coincides with the closure of the Mirovoi Ocean following the collision of a series of microcontinents with the Siberian craton, likely representing a typical record of collision-induced subduction jump. Our observations and numerical modeling provide a new scenario that subduction initiations would locate at oceanic weak zones rather than passive margins of accreted microcontinents during collision-induced subduction process.

Subduction initiation is among the most important processes in plate tectonics^{1–4}. There are two end-member mechanisms of subduction initiation: spontaneous and induced¹. Spontaneous subduction initiation originates from gravitational instability across oceanic transform faults, passive continental margins or mantle plume-head margins without plate convergence^{2,3,5–7}. Induced subduction initiation results from ongoing plate convergence following jamming of a subduction zone by buoyant crust, including jump (i.e. transference) and polarity reversal models^{1,3,8,9}. Only the subduction jump mechanism does not yet have an incontrovertible Cenozoic example^{3,10}, although this mechanism has been widely blamed for the successive terrane collision and consequent subduction initiation in the Tethyan realm^{10–14}. Numerical modeling results indicate that the subduction jump processes could be influenced by the compositional structure, rheological strength and width of allochthonous terranes, sediments around the accreting terranes, convergence rates, boundary convergence forces after terrane collision, and weak zones at passive continental margins of the

accreted terrane^{9,10,12,14,15}. However, the dynamic process of the subduction jump remains enigmatic, especially it struggles to explain why there are no signs of subduction initiation at the southern margin of Indian continent long after the India-Eurasia collision^{10,14}. Supra-subduction zone (SSZ) ophiolites are remnants of ancient oceanic lithosphere tectonically emplaced into orogenic belts and many of these ophiolites formed during subduction initiation in the proto-forearc setting^{16,17}. The spatio-temporal evolutionary characteristics of SSZ ophiolites throughout a whole orogen could provide insights into the geodynamic triggers, processes and lateral propagation of the subduction initiation^{18–21}.

The Central Asian Orogenic Belt (CAOB) is the largest known accretionary orogen^{22,23} (Fig. 1). Recent studies have suggested that the long-lived (1250–250 Ma) CAOB documents tectonic evolution of the Pan-Rodinian Mirovoi Ocean during Mesoproterozoic–Cambrian in the northern part overlapping that of the Paleo-Asian Ocean during Ediacaran–Triassic in the southern part^{24–26}. Several 1020–892 Ma SSZ

¹State Key Laboratory of Lithospheric and Environmental Coevolution, Institute of Geology and Geophysics, Chinese Academy of Sciences, Beijing, 100029, China. ²Key Laboratory of Mineral Resources, Institute of Geology and Geophysics, Chinese Academy of Sciences, Beijing, 100029, China. ³Instituto de Geociencias, Consejo Superior de Investigaciones Científicas, Madrid, Spain. ⁴Frontier Research Institute for Interdisciplinary Sciences, Tohoku University, Sendai, Japan. ⁵Department of Earth, Ocean and Atmospheric Sciences, University of British Columbia, 2020–2207 Main Mall, Vancouver, V6T 1Z4, Canada.

⁶Department of Geosciences, Swedish Museum of Natural History, Frescativägen 40, SE-104 05, Stockholm, Sweden. ⁷Key Laboratory of Petroleum Resource Research, Institute of Geology and Geophysics, Chinese Academy of Sciences, Beijing, China. ⁸Department of Mineralogy and Petrology, Georg-August-University Göttingen, Göttingen, Germany. ⁹School of Oceanography, Shanghai Jiao Tong University, Shanghai, 200030, China.

✉e-mail: zhumingshuai@mail.igcas.ac.cn; dongmiao@mail.igcas.ac.cn; shun.li@sjtu.edu.cn

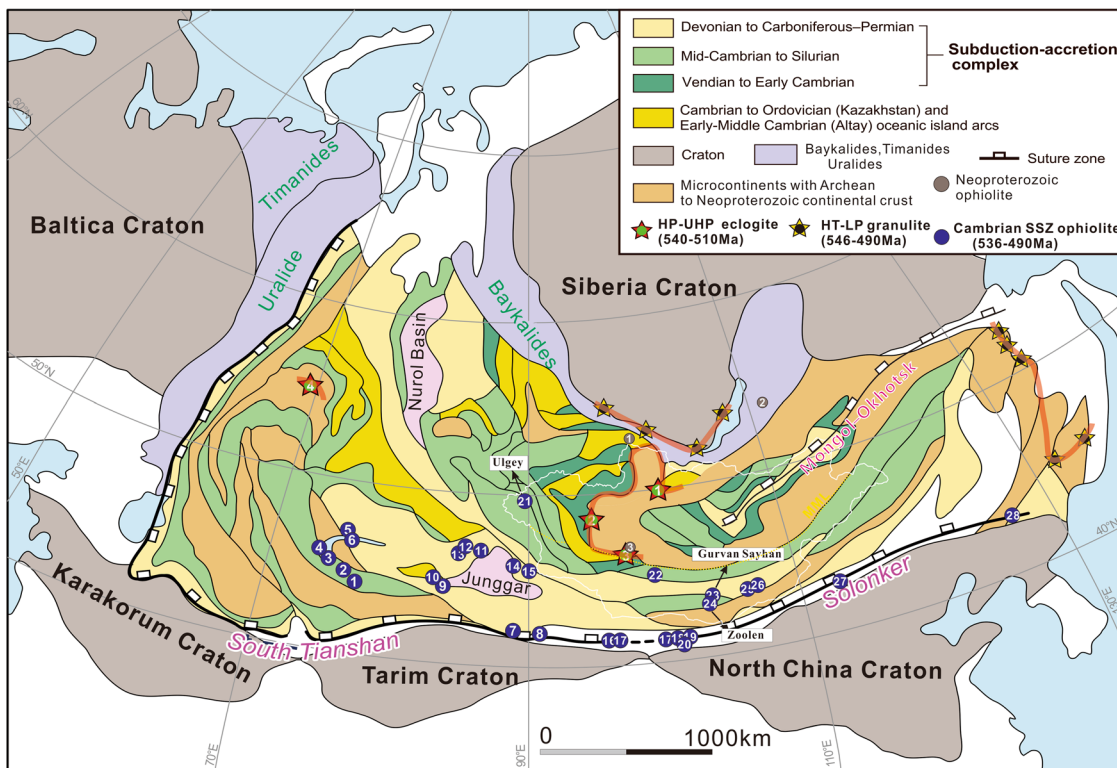


Fig. 1 | Tectonic map showing the Cambrian SSZ ophiolites and high-grade metamorphic belts of the CAOB. The main tectonic units of the CAOB are modified from Xiao et al.²³ and Zhu et al.²⁴. Cambrian HP-UHP metamorphic rocks (red stars): 1-Tsengel; 2-Urgamal; 3-Tsakhir Uul; 4-Kokchetav. The Cambrian granulitic metamorphic rocks along the margins of Siberian craton and the Khondalite belt in NE China are indicated by yellow stars. Cambrian SSZ ophiolites: 1-Kopurelisai; 2-Dulankara; 3-Sulu; 4-Andassai; 5-Tesikta; 6-Eastern Arkharsu; 7-

Gangou; 8-Kangguertage; 9-Tangbale; 10-Saleinuohai; 11-Hongguleleng; 12-Hebukesaier; 13-Chagantaolegai; 14-Zhaheba; 15-Aermantai; 16-Hongliuhe; 17-Yushishan; 18-Baiyunshan; 19-Xiaohuangshan; 20-Yueyashan; 21-Ulgey; 22-Gobi Altai; 23-Gurvan Sayhan; 24-Zoolen; 25-Namdain hundy; 26-Manlay; 27-Tulinkei; 28-Zhangjiatun-Toudaogou. Neoproterozoic ophiolites: 1-Dunzhugur; 2-Shamanka; 3-Erdene Uul.

ophiolites indicate that subduction of the Mirovoi Ocean initiated in the early Neoproterozoic^{26–28}. Cambrian continental-type eclogites reflect the closure of the Mirovoi Ocean at 548–520 Ma^{24,29,30}. The Paleo-Asian Ocean likely formed by the breakup of the Rodinian supercontinent between 750–600 Ma^{31,32}, and the oldest SSZ-type ophiolites and subsequent magmatic arc rocks in the southern CAOB indicate that subduction of the Paleo-Asian Ocean probably initiated in the Early Cambrian^{33–36}. Several mechanisms have been proposed to explain the subduction initiation in the Paleo-Asian Ocean: transform collapse³⁴, plume-induced³⁶ and arc-microcontinent collision³³. Whereas each of these mechanisms can explain theoretically the process of subduction initiation, they are mutually exclusive and may not work on a regional scale. The spatio-temporal evolution of the vast Paleo-Asian Ocean is underexplored and the geodynamic causes for subduction initiation within this domain are essentially unknown. In this paper, we document the discovery of three ophiolites with SSZ affinity in West Mongolia and present their stratigraphy, age and Hf isotope record, and whole-rock elemental composition. These data provide new records of subduction initiation of the Paleo-Asian Ocean in the West Mongolia segment. The compilation of Cambrian ophiolites in the CAOB and our numerical modeling studies yield new evidence for, and insights into, the collision-induced subduction initiation.

Results

Regional geology and sampling

The CAOB extends from the Uralides in the west to the Pacific margin in the east and is bound by the Siberian craton to the north and the Tarim–North China cratons to the south^{22,23} (Fig. 1). Mongolia is located in the heart of the CAOB and therefore provides an important geological record of how the

CAOB developed and how the various tectonic terranes relate to one another. Mongolia has been subdivided into two tectonic domains—the “Caledonian” domain to the north and the “Hercynian” domain to the south, separated by the Main Mongolian Lineament (MML)³⁷. The northern domain mainly consists of Precambrian microcontinents, Neoproterozoic–Cambrian subduction-accretionary complexes, early Paleozoic metamorphic rocks, and early Paleozoic sedimentary basins^{22,24,37}. In contrast, the southern domain comprises various mid- to late Paleozoic island arcs and ophiolite fragments, and Late Carboniferous to Permian volcanic rocks^{22,37}.

The Ulgey study area is located between the Altay and Khovd terranes, and is bounded by the Tolbo–Nuur and Khovd faults³⁸ (Supplementary Fig. 1). These two terranes mainly consist of Cambrian–Ordovician succession of clastic, volcaniclastic rocks and intermediate-mafic volcanic rocks, which are generally interpreted as a coherent accretionary volcano-sedimentary wedge developed during the subduction of oceanic lithosphere underneath Mongolian microcontinents^{39,40}. The Ulgey area mainly consists of Early–Middle Devonian volcanics and flysch-like sediments³⁸. Several dismembered ophiolitic fragments occur as inliers in fault contact with the Early–Middle Devonian formations³⁸. The ophiolite fragments mainly comprise serpentinized and carbonated harzburgite, pyroxenite, layered gabbro, isotropic gabbro, metabasalt, basaltic andesite and chert (Supplementary Fig. 2).

The Trans-Altai study area includes the Gurvan Sayhan and Zoolen ophiolitic mélange, which occur as dismembered fragments in a matrix dominated by Ordovician–Silurian greenschist-facies sedimentary and volcaniclastic rocks^{33,37} (Supplementary Fig. 3). The ophiolites consist of serpentinized harzburgite and lherzolite, wehrlite, gabbro, diabase, basalt, and minor diorite–tonalite–trondhjemite^{33,37} (Supplementary Fig. 4).

Hornblendites and diorites from the Gurvan Sayhan-Zoolen mélange yielded zircon U-Pb ages of 520–511 Ma³³. Geochemical data obtained from the ophiolite fragments so far do not provide exclusion regarding tectonic settings.

Whole-rock major and trace-element compositions (15 samples from the Ulgey ophiolite, 10 samples from the Gurvan Sayhan ophiolite and 11 samples from the Zoolen ophiolite) were determined by X-ray fluorescence (XRF) and ICP-MS, respectively. The results are presented in Supplementary Note 1 and Supplementary Tables 1–3. The major element compositions of Cr-spinels from the ultramafic rock of the Gurvan Sayhan ophiolite were analyzed using a JEOL JXA-8100 Electron Probe, and the results are presented in Supplementary Table 4. To obtain age estimates for the crust of the three ophiolites in West Mongolia, a gabbro from the Ulgey ophiolite, a plagiogranite from the Gurvan Sayhan ophiolite and a high-Mg diorite from the Zoolen ophiolite (detailed sample locations shown in Supplementary Fig. 1 and 3) were selected for in-situ U-Pb zircon dating using secondary ionization mass spectrometry. The zircon U-Pb age results are given in Supplementary Table 5. Zircon Hf isotope analyses for the gabbro sample from the Ulgey ophiolite were performed on the same spots as U-Pb age dating. The results are listed in Supplementary Table 6. The detailed analytical procedures can be found in the Methods Section.

Whole-rock geochemistry

The Ulgey ophiolite. The ultramafic rocks with variable degrees of serpentinization have high loss on ignition (LOI) values. They are characterized by low SiO₂ and alkalinity concentrations, and high MgO and Fe₂O₃^T concentrations, with Mg[#] [=molar Mg/(Mg + Fe²⁺)] ranging from 0.89 to 0.92. The gabbro samples exhibit chondrite-normalized light REE (LREE) enrichment (Fig. 2a₁), and are enriched in large-ion lithophile elements (LILEs; e.g., Sr, Ba, and U) and lack high field strength elements (HFSE) anomalies (Fig. 2a₂). The two basalt samples from the Ulgey

ophiolite have SiO₂ concentrations of 47.51 and 51.79 wt.%, MgO concentrations of 4.55 and 5.74 wt.%, Na₂O concentrations of 3.93 and 4.17 wt.% and TiO₂ concentrations of 0.78 and 0.99 wt.%. In the Zr/TiO₂ vs. Nb/Y diagram, the basalt samples plot in the basalt field, close to the forearc basalt (FAB) samples of Izu-Bonin-Mariana (IBM) forearc (Supplementary Fig. 5a). They show distinct LREE depletion [(La/Yb)_N of 0.44–0.60] and negligible Eu anomalies (Eu/Eu^{*} = 0.92 and 1.0) (Fig. 2a₁). The samples are slightly enriched in LILEs (e.g., Sr and Ba) and show minor negative anomalies in Nb and Ta, overlapping with the IBM FAB samples (Fig. 2a₂). The andesite samples have high MgO (4.04–6.64 wt.%) concentrations and Mg[#] (0.42–0.57). In the SiO₂-MgO diagrams (Supplementary Fig. 5b), all the samples plot in the high-Mg andesite (HMA) area, close to the HMA samples of the IBM arc. The samples show a positive slope with depletion of LREE [(La/Yb)_N = 0.29–0.75], slightly negative Eu anomalies (Eu/Eu^{*} = 0.79–0.96) (Fig. 2a₁) and negative Nb, Ta and Ti anomalies (Fig. 2a₂).

The Gurvan Sayhan ophiolite. The two ultramafic rocks with extensive serpentinization and alteration have high LOI values. They are characterized by low SiO₂, alkalinity concentrations, but high MgO, Mg[#] of 0.92. The concentrations of mantle compatible elements such as Cr and Ni are high in the ultramafic samples. The Cr-spinels from the ultramafic rock have relatively high Cr# (Cr# = Cr/(Cr + Al)) values (50–55) but low Mg# values (39–43) (Supplementary Table 4). Gabbro samples show flat REE patterns [(La/Yb)_N = 1.21 and 1.14] and negligible Eu anomalies (Eu/Eu^{*} = 0.98 and 0.88) (Fig. 2b₁). The samples show enrichment in LILEs (e.g., Sr and Ba) and depleted in Nb, Ta and Ti (Fig. 2b₂). The basalt samples show distinct enrichment of LREE [(La/Yb)_N = 4.3–7.9] relative to HREE with slightly negative Eu anomalies (Eu/Eu^{*} = 0.82–0.96) (Fig. 2b₁). These samples show enrichment in Ba, Th and Sr, but depleted in Nb, Ta and Ti (Fig. 2b₂).

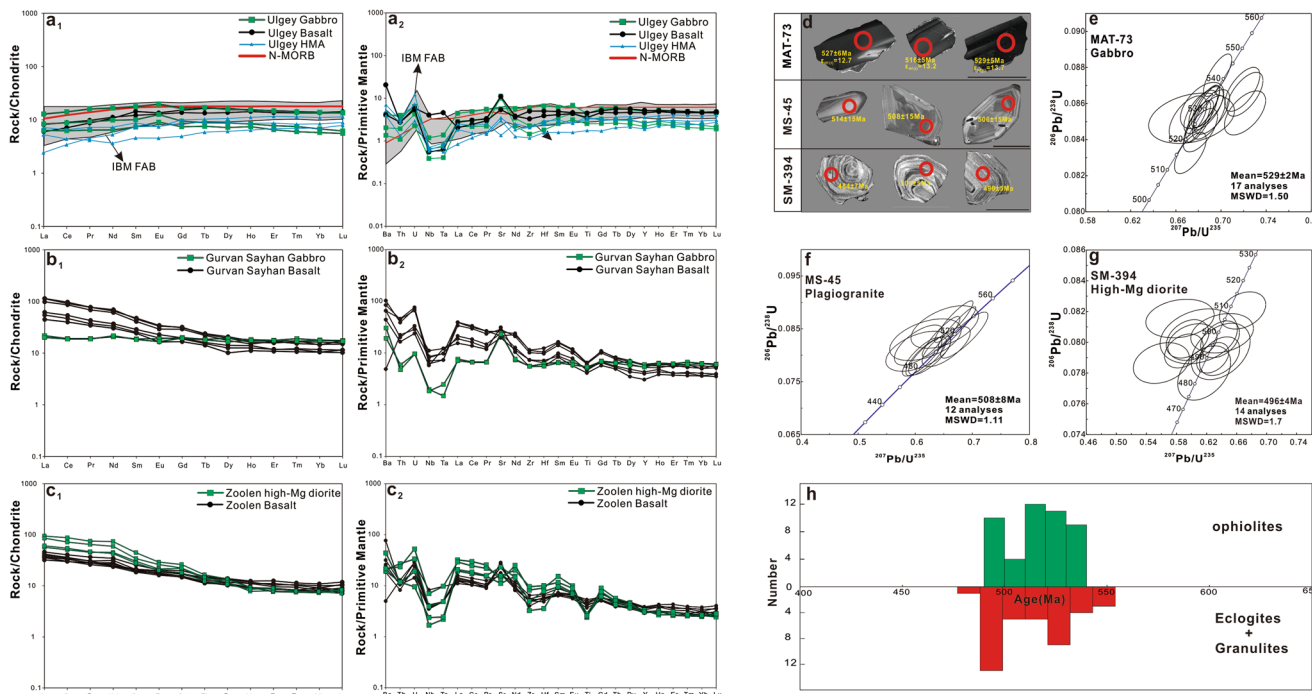


Fig. 2 | Geochemical diagrams and zircon U-Pb concordia diagrams for the Cambrian ophiolites in this study. **a₁, a₂** Chondrite-normalized REE patterns and primitive—mantle normalized diagrams for the Ulgey ophiolite. **b₁, b₂** Chondrite—normalized REE patterns and primitive-mantle normalized diagrams for the Gurvan Sayhan ophiolite. **c₁, c₂** Chondrite—normalized REE patterns and primitive-mantle normalized diagrams for the Zoolen ophiolite. **d** Representative CL images of zircons from the ophiolites. **e** Zircon U-Pb concordia diagram for the gabbro of the Ulgey ophiolite. **f** Zircon U-Pb concordia diagram for the plagiogranite of the Gurvan Sayhan ophiolite. **g** Zircon U-Pb concordia diagram for the high-Mg diorite of the Zoolen ophiolite. **h** Radiometric age histograms for the Cambrian ophiolites and high-grade metamorphic rocks in the CAOB. Geochemical normalizing values are from Sun and McDonough⁴³. Data sources of IBM forearc basalts are from Reagan et al.⁴⁴.

ophiolite. **f** Zircon U-Pb concordia diagram for the plagiogranite of the Gurvan Sayhan ophiolite. **g** Zircon U-Pb concordia diagram for the high-Mg diorite of the Zoolen ophiolite. **h** Radiometric age histograms for the Cambrian ophiolites and high-grade metamorphic rocks in the CAOB. Geochemical normalizing values are from Sun and McDonough⁴³. Data sources of IBM forearc basalts are from Reagan et al.⁴⁴.

The Zoolen ophiolite. The diorite samples have SiO_2 concentrations of 54.35–57.51 wt.% and MgO concentrations of 4.37–9.54 wt.% ($\text{Mg}^{\#} = 0.55\text{--}0.74$). In the $\text{SiO}_2\text{-MgO}$ diagrams, these samples plot in the HMA area (Supplementary Fig. 5b). They exhibit highly fractionated chondrite-normalized REE patterns with high LREE/HREE ratios [$(\text{La/Yb})_{\text{N}}$ of 7.40–12.83] and slight Eu negative anomalies ($\text{Eu/Eu}^* = 0.83\text{--}0.95$) (Fig. 2c₁). They show negative Nb, Ta, Zr, Hf and Ti anomalies (Fig. 2c₂). The basalt samples show moderate LREE enrichment [$(\text{La/Yb})_{\text{N}} = 3.89\text{--}4.39$] and nearly no Eu anomalies ($\text{Eu/Eu}^* = 0.83\text{--}0.94$) (Fig. 2c₁). These samples display enrichment in Ba, Th and Sr, but depleted in Nb, Ta, and Ti (Fig. 2c₂).

Zircon U-Pb geochronology. Zircons from the gabbro sample MAT-73 collected from the Ulgey ophiolite are euhedral to subhedral prisms that are 50–300 μm long. Most zircons show oscillatory zoning (Fig. 2d), which is characteristic of igneous zircon⁴¹. Zircon U and Th concentrations are between 236–1913 ppm and 126–3177 ppm, respectively. The Th/U ratios are between 0.53 and 1.98, also indicating an igneous origin⁴¹. The analyses yield a weighted mean $^{206}\text{Pb}/^{238}\text{U}$ age of 529 ± 2 Ma (MSWD = 1.5; Fig. 2e), which is interpreted as the crystallization time of zircons. Six zircon grains were selected for Hf isotope analysis. The analyses yielded positive $\epsilon_{\text{Hf}}(\text{t})$ values (+12.5–+15.0), which yield young model ages T_{DM} (537–700 Ma).

Zircon grains from the plagiogranite sample MS-45 collected from the Gurvan Sayhan ophiolite are euhedral prisms that are 100–200 μm long (Fig. 2d). Most zircons show well-developed oscillatory zoning. Twelve zircon grains were chosen for analysis. The measured U and Th concentrations vary from 104–661 ppm and from 14–190 ppm, respectively, with Th/U ratios between 0.14 and 0.39. All the analyses yield a weighted mean $^{206}\text{Pb}/^{238}\text{U}$ age of 508 ± 8 Ma (MSWD = 1.1; Fig. 2f), which is interpreted as the zircon crystallization age.

Zircon grains from the high-Mg diorite sample SM-394 collected from the Zoolen ophiolite are relatively euhedral, and their CL images show well-developed oscillatory zoning (Fig. 2d). Fourteen zircon grains were analyzed. The U and Th concentrations are 66 to 228 ppm and 109 to 114 ppm, respectively. The Th/U ratios are between 0.50 and 1.72. All the analyses yielded a weighted mean $^{206}\text{Pb}/^{238}\text{U}$ age of 496 ± 4 Ma (MSWD = 1.7; Fig. 2g), which can be interpreted as the time of zircon crystallization.

Discussion

Age and tectonic setting of the ophiolites

The Ulgey ophiolite is ascribed to the Late Neoproterozoic–Early Cambrian on the Geological Map of Central and Western Mongolia, Scale 1:500,000⁴². However, no age data have been reported for the ophiolite. The gabbro from the ophiolite yielded a zircon U–Pb age of 529 ± 2 Ma, which shows that the Ulgey ophiolite formed during the Early Cambrian. The plagiogranite and high-Mg diorite fragments from the Gurvan Sayhan–Zoolen ophiolitic mélanges yielded SHRIMP zircon U–Pb ages of 508 ± 8 Ma and 496 ± 4 Ma, which are comparable with the ages of the fragments from these two ophiolitic mélanges (520–511 Ma)³³, indicating the Gurvan Sayhan–Zoolen ophiolitic mélanges are formed during Cambrian.

The radiogenic Hf isotope compositions of the gabbro and the depleted mid-ocean ridge basalts (N-MORB) geochemical features of the basalt from the Ulgey ophiolite suggest their origin from a depleted mantle reservoir⁴³. However, compared with MORB, the basalt samples show lower HFSE concentrations (Nb and Ta), which are comparable to FABs^{44,45}. They also exhibit slight enrichment in LILEs (Ba and U) that are not positively correlated with the LOI, indicating some inputs of slab-derived material rather than the effect of the alteration⁴⁶. This inference is reinforced by Nb/Yb and Th/Yb values of the basalt samples, which are slightly higher than those of the mantle array (Supplementary Fig. 6a). All these data suggest that the basaltic rocks from the ophiolites show geochemical affinities to FABs, which are considered the first lavas to erupt after subduction initiation^{44,47}. The Ulgey high-Mg andesites have geochemical affinities to typical HMAs. The HMAs are generally divided into four subtypes: high-Mg adakite,

bajaite, boninite and sanukitoid^{48,49}. The low Sr concentrations, Sr/Y and $(\text{La/Yb})_{\text{N}}$ of the Ulgey HMAs distinguish these rocks from high-Mg adakites and Bajaites (Supplementary Fig. 6b). They yield lower MgO, higher TiO_2 and Y concentrations compared to the typical boninites⁵⁰. The high TiO_2 and Y concentrations, but low Sr/Y and $(\text{La/Yb})_{\text{N}}$ of the Ulgey HMAs indicates that they are analogous to sanukite, similar to the HMAs from the IBM arc (Supplementary Fig. 6b). Combined with their arc-type geochemical characteristics, we suggest the Ulgey HMAs originated from partial melting of the mantle wedge modified by interaction with a subducting slab^{51,52}. The high-Mg andesites display enrichment of LILEs and LREEs and distinct depletion of HFSEs, indicating slab input as also seen in the HMAs from the IBM arc^{44,47,50}.

The enrichment in LREE and LILE, and negative Nb, Ta and Ti anomalies and Nb/Yb–Th/Yb compositions (Supplementary Fig. 6a) of the gabbros and basalts from the Gurvan Sayhan–Zoolen ophiolitic mélanges also indicate an origin in a subduction zone setting. Such ophiolites could form in a back-arc or forearc settings⁵³. The composition of Cr-spinel from the peridotite could document the degree of partial melting of the mantle source, and thus provide additional constraints on the tectonic setting of the SSZ ophiolites^{18,54}. The Cr-spinels from the Gurvan Sayhan–Zoolen have relatively high Cr[#] values but low Mg[#] values, and exclusively plot in the forearc tectonic setting field (Supplementary Fig. 7). The low Sr/Y of the Zoolen high-Mg diorites distinguishes them from high-Mg adakites and Bajaites (Supplementary Fig. 6b). One of these high-Mg diorite samples (sample SM-400) shows similar features to boninite formed in forearc tectonic setting¹⁵, while other samples have features analogous to those of sanukites (Supplementary Fig. 6b). In addition, the high-Mg diorites from the Zoolen ophiolitic mélanges show typical arc-type geochemical features, indicating they resulted from partial melting of the mantle wedge modified by a subducting slab⁵¹. Our studies suggest that the Gurvan Sayhan–Zoolen ophiolitic mélanges represents an intra-oceanic arc during Cambrian.

SSZ ophiolites are widely interpreted to record forearc extensions of the upper plate during subduction initiation^{16–20}, and are characterized by a stratigraphic chemical progression (from bottom to top) from less to more HFSE-depleted and LILE-enriched compositions, adhering the ‘subduction initiation rule’^{16–18}. Specifically, the volcanic crustal section of the SSZ ophiolite should comprise earliest MORB-like FABs, followed by boninites and other HMAs, and finally arc tholeiites and calc-alkaline rocks^{16,17}. According to the studies of the IBM intra-oceanic arc system, the transition from FABs to boninitic volcanism takes 2–4 Myr⁵⁵. The diagnostic FABs and/or boninitic components in the SSZ ophiolites are thought to represent initial volcanism associated with subduction initiation^{16–18,33,35}, even though ophiolite chemostratigraphic records are frequently dismembered and incomplete^{16,56}. Thus, the ~529 Ma Ulgey ophiolite with a magmatic sequence akin to that in the IBM forearc, and the 508–496 Ma Gurvan Sayhan–Zoolen ophiolitic mélanges with boninitic magmatism likely document the formation of new ophiolitic crust associated with diachronic subduction initiation of the Paleo-Asian Ocean in the West Mongolia segment.

Diachronic Cambrian subduction initiation of the Paleo-Asian Ocean

The CAOB generally grew gradually southward as evidenced by the ophiolitic mélanges showing a younging trend from north to south^{22,56}. The transition from the Mirovoi Ocean to Paleo-Asian Ocean tectonic domains in the CAOB occurred at ca. 548–520 Ma²⁴. Thus, the Neoproterozoic ophiolites (ca. 1020–570 Ma)^{26–28,33} in the northern part of the CAOB are likely related to the evolution of the Mirovoi Ocean, and the Cambrian–Permian ophiolites^{22,23,25,33–35} in the southern part of the CAOB are related to evolution of the Paleo-Asian Ocean. The SSZ ophiolites in the CAOB (Fig. 1, Fig. 2h and Supplementary Table 7) suggest that the subduction of the Paleo-Asian Ocean initiated ca. 532–513 Ma in the Kazakhstan segment (Tesiktaš, Eastern Arkharsu and Djalar-Naiman ophiolites)^{35,57}, at 531–496 Ma in the Junggar segment (Tangbale-Mayile, Kujibai-Hongguleleng and Zhaheba-Aermantai ophiolite belts)^{34,58,59}, at

536–496 Ma in the East Tianshan–Beishan segment (Kangguertage, Gangou, Hongliuhe–Niujuanzi–Xichangjing and Jijitaizi–Xiaohuangshan ophiolite belts)^{60–62}, at ca. 529–494 Ma in the West Mongolia segment (Ulgei, Gobi Altai and Gurvan Sayhan-Zoolen ophiolite belts) (this study and ref. 33), at ca. 528–509 Ma in the East Mongolia segment (Manlay-Namdain hundy ophiolite belt)^{63,64}, at ca. 530–491 Ma in the East Inner Mongolia-Central Jijin segment^{65,66}. Though not all Cambrian SSZ ophiolites described in the literature follow the ‘subduction initiation rule’, FABs and/or boninite components identified in these ophiolites, especially the oldest ophiolites, suggest they were formed during the onset of subduction^{33,35,61,62,64} (Supplementary Fig. 8). For example, the gabbros from Tesiktas ophiolite and Eastern Arkharstu ophiolite in the Kazakhstan segment show boninite-like characteristics³⁵. The basalts from the Tangbale ophiolite, Mayile ophiolite, Barleik ophiolite and Saleinuohai ophiolite in the Junggar segment display geochemical features similar to those of FABs from the IBM arc^{36,67}. The basalts and gabbros from the Gangou ophiolite in the East Tianshan region show geochemical affinities to those of transitional FABs and boninites⁶², and the basalts from the Xichangjing, Hongliuhe and Yushishan ophiolites in the Beishan region show geochemical features similar to those of the FABs⁶¹. The basalts from the Namdain hundy ophiolite in the East Mongolia, and the basalts from Toudaogou ophiolite and Tulinkai ophiolite in the East Inner Mongolia-Central Jijin have geochemical affinities to the FABs^{64–66}. Thus, the oldest ophiolites in different segments of the CAOB suggest that subduction of the Paleo-Asian Ocean was initiated diachronically at 536–528 Ma along a new convergent plate boundary that was over 6000 km long (Fig. 1).

Subsequent to the subduction initiation, Late Cambrian to Early Ordovician island arc complexes have been identified in different segments of the Paleo-Asian Ocean (Supplementary Fig. 9). In the Kazakhstan segment, Bozshakol-Chingiz arc (501–480 Ma; about 1470 km long) mainly consist of basalt, andesite, dacite and various granodiorite plutons with typical subduction-related geochemical features^{68–70}. This Late Cambrian–Early Ordovician island arc is located north to the Early Cambrian SSZ ophiolites, indicating a northward subduction polarity of the Paleo-Asian Ocean³⁵. In the Junggar segment, extensive Late Cambrian tholeiitic–calc-alkaline subduction-related plutons (515–485 Ma) marked the transition from an immature arc to a mature one^{34,36,67}. The immature island arc developed to the south of the SSZ ophiolites, and the arc magmatism in the west Junggar migrated from south to north due to rollback of the subducted slab, favoring a southward subduction polarity³⁴. In the Tianshan–Beishan segment, Late Cambrian–Early Ordovician subduction-related calc-alkaline diorites and granites (510–470 Ma) are identified in the Aktyuz region of the Western Tianshan⁵⁸, southern margin of the Yili Block⁷¹ and Beishan Gongpoquan arc⁷², recording a mature island arc tectono-magmatic setting (about 1800–2000 km long). The island arcs are mainly located to the north of the Early Cambrian SSZ ophiolites^{62,63}, indicating the Paleo-Asian Ocean subducted from south to north in this segment⁶³. In the West Mongolia segment, Late Cambrian–Early Ordovician subduction-related calc-alkaline metagabbros, dioritic to granitic orthogneisses (520–467 Ma) are recognized in the Hovd Zone of western Mongolia, Gurvan Sayhan-Zoolen region and Gobi-Altai region of southwestern Mongolia, which likely constitute part of a 1200 km long island arc belt^{33,73,74}. Despite that the arc system has been modified by later tectonic deformation³⁷, this island arc is mainly developed to north of the SSZ ophiolites likely associated with a northward subduction of the Paleo-Asian Ocean³³. In the East Mongolia segment, the calc-alkaline basalt, andesite and dacite of the Huree island arc (ca. 487 Ma), and the adakites intruding the ophiolites (503–491 Ma) represent the younger arc magmatism following the subduction initiation^{64,65}. The spatial configuration of the SSZ ophiolites, island arc and back-arc basin belt suggests that the subduction polarity of the Paleo-Asian Ocean was from south to north, forming a trench-arc-basin system south of the Central Mongolia microcontinent^{64,65}. In the East Inner Mongolia-Central Jijin segment, the Bainaimiao arc (520–420 Ma), mainly composed of subduction-

related volcanic rocks (basalt, rhyolite and volcanic breccia) and intrusive rocks (quartz diorite and tonalite), extends over 1300 km from the Bayan Obo area, through the Bainaimiao and Jiefangyingzi areas in Inner Mongolia, to eastern Siping and Yitong area in Jilin Province^{75,76}. The spatiotemporal distribution of SSZ ophiolites, arc magmatism and sedimentary formations within Inner Mongolia–Jilin region support a southward subduction of the Paleo-Asian Ocean⁶⁷. The Cambrian SSZ ophiolites and subsequent younger arc magmatic rocks suggest new subduction zones formed with varied subduction polarities during early Cambrian in different segments of the Paleo-Asian Ocean. Several hypotheses have been proposed to account for the Cambrian subduction initiation of the Paleo-Asian Ocean^{33,34,36}. For example, Ren et al.³⁴ and Yang et al.³⁶ proposed that Cambrian subduction initiation of the Paleo-Asian Ocean in the Junggar segment was related to a transform collapse or a mantle plume, respectively. Jian et al.³³ proposed that subduction of the Paleo-Asian Ocean in the West Mongolia segment initiated due to the arc-continent collision. The abovementioned hypotheses for subduction initiation in the Paleo-Asian Ocean^{33,34,36} can explain the formation of new subduction zones on a local scale. However, applying these models to explain the rapid nucleation (<8 Myr) of such an extensive subduction zone (over 6000 km long) presents significant challenges. Development of such an extensive convergent boundary would require and signify large-scale changes in kinematics of the regional to global plate circuit.

During Cambrian, the Mirovoi Ocean fully closed after multiple microcontinents collided with the Siberian craton²⁴ (Fig. 3). The newly-identified >1000 km long Cambrian HP metamorphic belt (ca. 548–520 Ma)^{24,29,30} provides a HP/LT (low-temperature) complement to the previously identified Cambrian granulite-facies metamorphism and HP metamorphism that has affected the southern margin of the Siberian craton and various microcontinents across the CAOB (Figs. 1, 2h and Supplementary Table 8), for instance the >1300 km long Cambrian granulite-bearing Khondalite Belt of NE China (530–500 Ma)^{77,78}, the >1000 km long granulite-bearing metamorphic belt at the southern margin of the Siberian craton (507–490 Ma)⁷⁹ and the >150 km long Kokchetav continent-type HP and ultrahigh-pressure (UHP) terrane (540–510 Ma)^{80,81}. Such a scenario is supported by palaeomagnetic data that indicates that the CAOB microcontinents were adjacent to the Siberian craton during the early Cambrian⁸². These high-grade metamorphic belts represents a continental subduction front (possibly >3500 km) during the microcontinents collision with the Siberian craton. Given the timing of initial subduction of the Paleo-Asian Ocean coincides well with the timing of closure of the Mirovoi Ocean (Fig. 2h), we argue that the steering of the Paleo-Asian Ocean plate and corresponding subduction initiation(s) may have been induced by the collision of microcontinents with the Siberian craton (Fig. 3). We think that a simultaneous initiation of the subduction of the Paleo-Asian Ocean along a 6000 km long convergent plate boundary is very unlikely. However, it is plausible that subduction initiated diachronically at some points between 536–528 Ma and then gradually formed during the Cambrian–Ordovician. The along-strike variations of SSZ ophiolites in each segment of the CAOB likely trace the lateral propagation of subduction initiations (also called subduction invasion) through space and time^{19,83,84} (Fig. 3b), although other mechanisms of subduction initiation and geodynamic settings of ophiolite formation could not be precluded.

Temporally overlapping with the Cambrian orogenesis around the southern margin of the Siberian craton, a series of kinematically interlinked peripheral orogens (Terra Australis, Avalonian–Cadomian and North Indo-Australie orogens) formed around the margins of Gondwana^{32,85,86} (Fig. 3a). The timing of initial subduction of the Paleo-Asian Ocean surrounding the Siberian craton coincides well with the timing of proposed slab rollback and subduction initiation of the oceans (Proto-Pacific, Iapetus and Proto-Tethys oceans) surrounding the Gondwana supercontinent^{87–89} (Fig. 3a). This global scale subduction system and enhanced weathering flux of the Cambrian peripheral orogens would increase the subduction efficiency of cold lithosphere into the deep mantle, and thus lead to rapid cooling of Earth

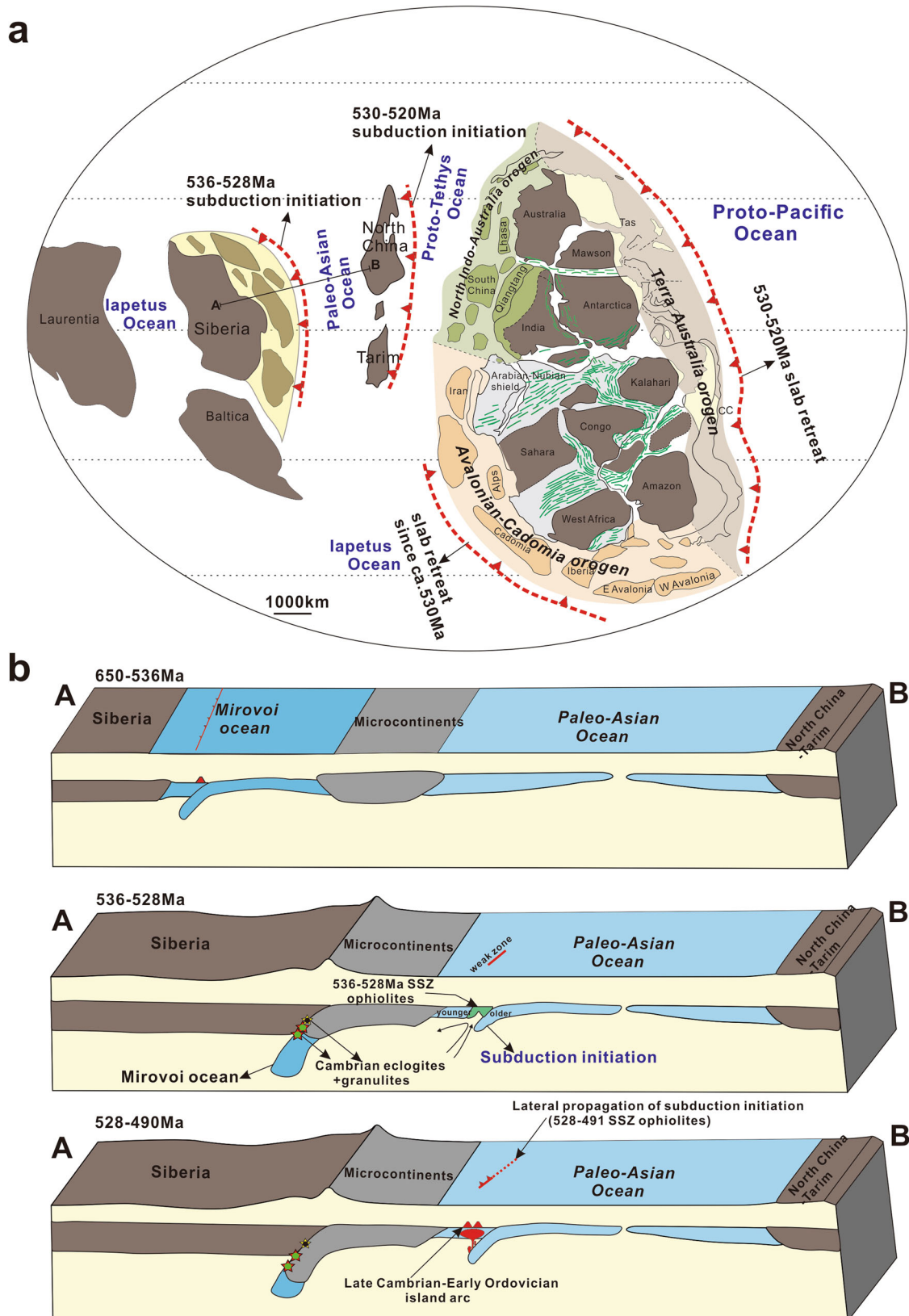


Fig. 3 | Tectonic reconstruction of the collision-induced subduction initiations of the Paleo-Asian Ocean during Cambrian. a Global paleogeographic reconstruction during Cambrian (modified from Zhao et al.³², Cawood et al.⁸⁵ and Zhu et al.²⁴).

b Schematic diagrams for the tectonic evolution of the CAOB during Neoproterozoic to Cambrian.

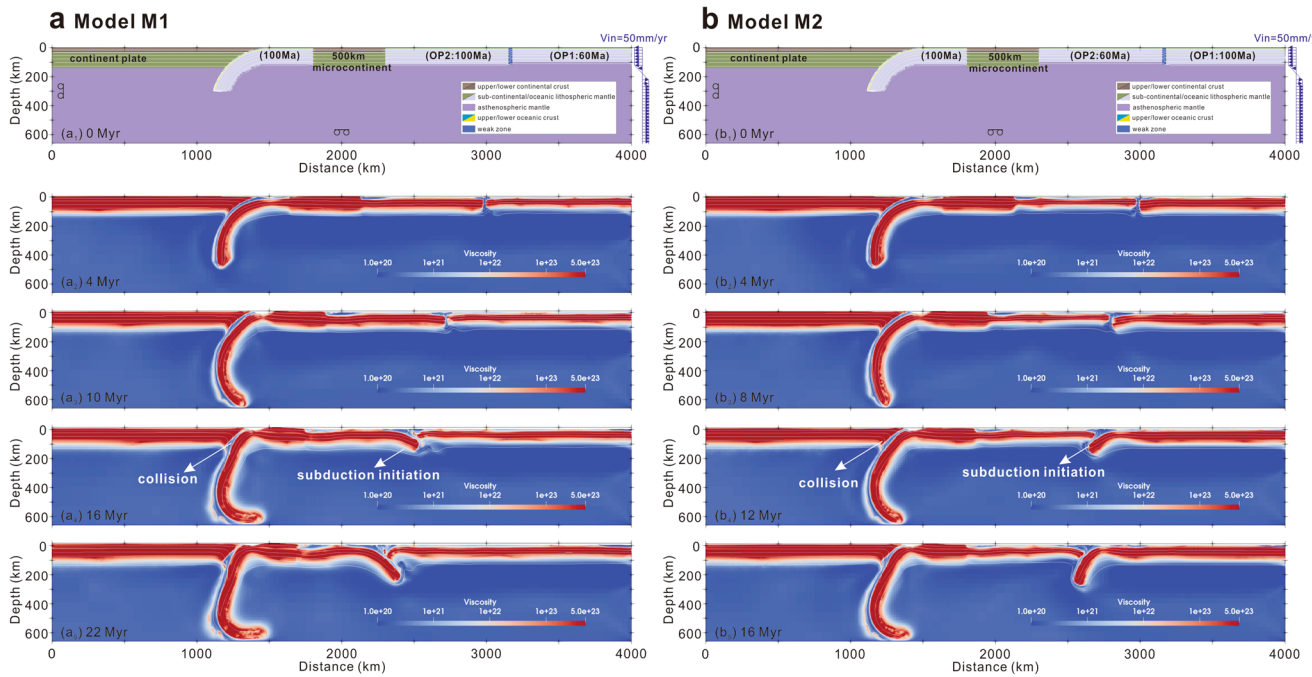


Fig. 4 | Model setup and numerical model evolution of viscosity showing subduction initiations along the weak zone in collision-induced subduction initiation processes. **a** Setup and numerical model evolution of Model M1. **b** Setup and numerical model evolution of Model M2.

as evidenced by the dramatic drop of mean thermobaric ratios T/P ratio during Cambrian^{88,89}.

Implications for the collision-induced subduction jump

Previous studies have proposed that, during a collision-induced subduction jump, subduction initiation would occur at the passive margin of accreted microcontinents^{10,14}. However, most Cambrian SSZ ophiolites in the CAOB were located far from the margins of microcontinents^{33–36,62,63} (Fig. 1). Subduction initiation in the Paleo-Asian Ocean thus appears to have taken place at the weak intra-oceanic zones, such as transform faults and oceanic fracture zones, rather than at the outboard passive margins of the accreted microcontinents. In order to test this hypothesis, we conducted a series of numerical models with the finite element code ASPECT^{90–92}. The models consist of four tectonic units: a continent plate on the left side, and a microcontinent surrounded by two oceanic plates, as shown in Fig. 4a₁ and b₁. The oceanic plate on the right side of the model is separated by an initial 30 km-wide weak zone into two parts (OP1 and OP2) with different ages. Model M1 set includes OP1 of 60 Ma in contrast to OP2 of 100 Ma, and Model M2 set includes OP1 of 100 Ma in contrast to OP2 of 60 Ma (Fig. 4a₁, b₁). The oceanic plate on the right side is neighbored by a drifting microcontinent terrane (500 km) with passive margins on both sides. A preexisting subduction zone was set between the oceanic plate of 100 Ma on left side and the continent plate. Detailed model parameters and boundary conditions could be found in the Methods and Supplementary Table 9. Our model results suggest that the microcontinent would collide with the continent plate within 16 Ma as the prescribed subduction proceeds (Fig. 4 and Supplementary Movies). Immediately after the initial microcontinent–continent collision, a new subduction zone begins to form at the weak zone within the oceanic plate rather than the outboard passive margin of the accreted microcontinent, and the older part of the oceanic plate would subduct beneath the younger part (Fig. 4 and Supplementary Movies). Our numerical models suggest that the passive margins of the accreted microcontinents had the rheological strength to resist lithospheric collapse during collision-induced subduction initiation process, unless they were sufficiently weakened^{7,10,83,93}. Previous numerical modeling studies indicate that the force required for collision-induced subduction initiation at passive margins that lack a weak zone is estimated

to be above 8.0×10^{12} N/m, whereas subduction initiation at a pre-existing weak zone is estimated to be about half that^{10,94}. Thus, we suggest that oceanic weak zones are more inclined to accommodate subduction initiation during a collision-induced subduction jump than the strong passive margins of microcontinents. The oldest Cambrian ophiolites in each segment of the Paleo-Asian Ocean represent starting sites of subduction initiation in the weak zones as demonstrated in our two-dimensional (2D) numerical modeling. After starting, the subduction initiation would propagate laterally along the weak zone driven by both the negative buoyancy and the pull of the neighboring subducted slab¹⁹, which has been previously investigated by means of three-dimensional (3D) thermomechanical modeling^{19,83}. Subduction initiation propagation along weak zones is suggested to be a common geodynamic process in the Cenozoic subduction systems^{83,84} (e.g., the New Hebrides and Macquarie-Puysegur), and has been used to explain the spatial-temporal distribution of Cretaceous SSZ ophiolites along the suture zone (>3000 km) of the Neotethyan Ocean¹⁹. Thus, we suggest that the distribution of SSZ ophiolites with different ages likely record the lateral propagation of subduction initiation in different segments of the Paleo-Asian Ocean. In addition, we propose, according to our numerical models, that the varied Cambrian subduction polarities in different segments of the Paleo-Asian Ocean resulted from age difference of the oceanic plates on the sides of the weak zones, where the older oceanic plates would underthrust beneath the younger ones.

The numerical modeling and observations made in this study shed new lights on the collision-induced subduction jump within the Tethyan realm, where a series of microcontinents continuously drifted from Gondwana in the south to form new oceans, and accreted to the Eurasian continent in the north to close the preexisting oceans since Paleozoic^{10,95,96}. During this process, the collisions between the Gondwana-derived microcontinents and Eurasian continent are suggested to have induced the subduction initiation of new oceans^{10,11,14,96}. The geodynamic processes of the collision-induced subduction jump within the Tethyan realm remain elusive. It is especially unclear why no subduction zone initiated along the southern passive margins of the India continent even though the India-Asia collision had already occurred ca. 50 Ma ago^{3,10,11}. Our study indicates a new scenario in which subduction initiation during a collision-induced subduction jump

would locate at oceanic weak zones rather than the passive margins of the accreted continents and/or microcontinents. Recent studies have proposed that the India-Asia collision induced the synchronous Cenozoic subduction initiations at places with lithospheric weaknesses within the west Pacific Ocean through lever effect⁹⁷, which is consistent with our new model. This mode of post-accretion subduction initiation generates laterally extensive convergent margins in oceanic basins subjected to far-field compression or transpression.

Methods

Whole-rock geochemistry

Whole-rock major and trace element compositions were determined at the Wuhan Sample Solution Analytical Technology Co., Ltd., China. Fresh samples were crushed and subsequently reduced to powder in an agate shatter box. Major oxides were analyzed in fused glass disks using an X-ray fluorescence spectrometer (XRF-1800). The precision is within $\pm 2\%$ for the oxides >0.5 wt.% and within $\pm 5\%$ for the oxides >0.1 wt.%. Whole-rock trace element analyses were performed by inductively coupled plasma mass spectrometry (ICP-MS). Samples were dissolved by a mixed acid of HNO_3 and HF in a Teflon vessel, and in high-pressure Teflon bombs at 120 °C for 6 days. The solution was evaporated to incipient dryness, dissolved by concentrated HNO_3 and evaporated at 150°C to dispel the fluorides. The samples were diluted to about 80 g for analysis after re-dissolved in 30% HNO_3 overnight. The signal drift of the spectrometer was monitored by an internal standard rhodium solution. Analytical results for USGS standards indicated that the uncertainties during trace element analysis for most elements were within 5%.

Cr-spinel chemistry

Major element compositions of the Cr-spinels were analyzed on a JEOL JXA-8100 Electron Probe with four wavelength dispersive spectrometers at the Institute of Geology and Geophysics, Chinese Academy of Sciences (IGGCAS), applying a 15 kV accelerating voltage and a 10 nA beam current. Count times were 10 s on peaks, and 5 s on each background. Natural minerals and synthetic oxides were used as standards. A program based on the ZAF procedure was used for data correction.

Zircon U-Pb geochronology

Zircon grains were separated from the crushed samples by conventional heavy liquid and magnetic separation technique. These grains were mounted with zircon standards in epoxy mount and polished to expose the zircon interiors. Transmitted and reflected light microphotographs and cathodoluminescence (CL) images obtained using a HITACHI S-3000 N SEM were prepared to investigate internal texture and origin of the zircons.

Zircon U-Pb analysis by the SHRIMP secondary ionization mass spectrometry instrument was performed at the Beijing SHRIMP Center, Institute of Geology, Chinese Academy of Geosciences. The spot size of the ion beam was about 20 μm and the intensity of the primary O_2^- ion beam was 4–6 nA. Each spot was rastered for 3 min prior to analysis to remove surface common Pb. The analytical data were processed using the Excel-based programs SQUID 1.03⁹⁸ and ISOPLOT 3.0⁹⁹. Common Pb corrections used the measured ^{204}Pb and the ^{204}Pb -based methods of Compston et al.¹⁰⁰. Weighted mean ages of individual samples are quoted at the 95% confidence level (2σ).

Zircon Hf isotope

In situ zircon Lu-Hf isotopes were carried out by the MC-ICP-MS at the Beijing Createch Testing Technology Co. Ltd. The laser ablation beam spot is 40 μm in diameter, and the analyzed pulse frequency of the laser beam is 8 Hz. Detailed analytical procedures are described in ref.¹⁰¹. In the calculation of the $\epsilon\text{Hf}(t)$ values, the $^{176}\text{Hf}/^{177}\text{Hf}$ and $^{176}\text{Lu}/^{177}\text{Hf}$ ratios of present-day chondrite and the depleted mantle were (0.0332, 0.282772) and (0.0384, 0.28325), respectively¹⁰². The $^{176}\text{Hf}/^{177}\text{Hf}$ value of the standard zircon Plešovice tested in this experiment was 0.282480 ± 0.000016 (2σ), which is consistent with the value of the predecessor¹⁰³ within the error range.

Numerical modeling

Model setup. The model geometry is 4000 km by 660 km. The left side of the model represents the continental plate, which is 1500 km wide. The microcontinent is 500 km wide and is located in the middle of the model. Both the microcontinent and the continental plate in the models are composed of a 20 km thick felsic upper crust, a 15 km thick mafic lower crust, and a 105 km thick lithospheric mantle. The initial temperature settings increase from 0 °C to 1300 °C in thermal equilibrium. Between the continent and the microcontinent, there is a subducted oceanic plate. To the right of the microcontinent, there is also an oceanic plate, which is initiated with a 30 km wide weak zone in the middle of this oceanic plate. All the oceanic plates contain an upper crust (4 km thick) to facilitate subduction and a layer of lower crust (6 km thick). The thickness and initial temperature of the mantle lithosphere depend on the age and are controlled by half-space cooling. The initial temperature gradient in the asthenospheric mantle is about 0.5 °C/km. The thermal boundary conditions have a fixed value of 273 K for the top boundary. The left and bottom boundaries of the model are free-slip, while the right boundary is set to a speed boundary. The convergence rates of oceanic plates are 5.0 cm/yr in the models. The outflow velocity is also set at the right boundary to maintain material balance. The top boundary is set as a free surface, which is controlled by mesh deformation.

Governing equations. Pressure and velocity are solved for using the extended Boussinesq equations of momentum and mass. Thermal evolution is modeled through the advection-diffusion equation. Compositional fields are used to track and advect distinct lithologic domains and other time-dependent quantities. Each field requires solving an additional advection equation. Equations used are as follow:

$$-\nabla \cdot 2\eta\dot{\epsilon} + \nabla P = \rho g \quad (1)$$

$$\nabla \cdot \mathbf{u} = 0 \quad (2)$$

$$\rho C_p \left(\frac{\partial T}{\partial t} + \mathbf{u} \cdot \nabla T \right) - \nabla \cdot K \nabla T = \rho H \quad (3)$$

$$\frac{\partial c_i}{\partial t} + \mathbf{u} \cdot \nabla c_i - \nabla \cdot \nu \nabla c_i = 0 \quad (4)$$

where η is the effective viscosity (see Eqs. (5)–(7)), $\dot{\epsilon}$ is the deviatoric strain rate tensor, which is given by $\frac{1}{2}(\nabla \mathbf{u} + (\nabla \mathbf{u})^T)$, P is the pressure, ρ is the density, which is defined as $\rho = \rho_0(1 - \alpha(T - T_0))$ with T_0 being the reference temperature (293 K), g is the gravitational acceleration, \mathbf{u} is the velocity, C_p is the specific heat capacity, T is the temperature, t is time, K is the thermal conductivity, and H is the volumetric heat source term that includes radiogenic heat, shear heating, and adiabatic heating. ν is the artificial diffusion, c_i represents each Eulerian compositional field.

Rheology. We use the Drucker–Prager yield criterion and a visco-plastic rheology¹⁰⁴ with dislocation and diffusion creep, which are incorporated into ASPECT via the following equations:

$$\eta_{comp} = \left(\frac{1}{\eta_{diff}} + \frac{1}{\eta_{disl}} \right)^{-1} \quad (5)$$

$$\eta_{diff} = \frac{1}{2} A_{diff}^{-1} d^m \exp \left(\frac{E_{diff} + PV_{diff}}{RT} \right) \quad (6)$$

$$\eta_{disl} = \frac{1}{2} A_{disl}^{-\frac{1}{n}} (\dot{\epsilon}_{II})^{\frac{1-n}{n}} \exp \left(\frac{E_{disl} + PV_{disl}}{nRT} \right) \quad (7)$$

where η_{comp} is the composite viscosity, η_{diff} is the diffusion creep, η_{disl} is the dislocation creep, A is the pre-exponential factor, n and m are stress and

grain size exponents, $\dot{\varepsilon}_{II}$ is the second invariant of the strain rate tensor, which is defined as $\dot{\varepsilon}_{II} = (0.5\dot{\varepsilon}_{ij}\dot{\varepsilon}_{ij})^{0.5}$, E is the activation energy, V is the activation volume, R is the gas constant. These parameters are determined from the flow law experiments (Table S9).

Frictional-plastic deformation is responsible for faulting and follows a pressure-dependent Drucker–Prager yield criterion:

$$\sigma_{yield} = \frac{6C_0 \cos \varphi + 6P \sin \varphi}{\sqrt{3(3 + \sin \varphi)}} \quad (8)$$

where σ_{yield} is the yield stress, C_0 is the cohesion, and φ is the angle of internal friction.

Data availability

Supplementary information, Supplementary data (Table S1–S9) and Supplementary movies have been deposited in <https://doi.org/10.5281/zenodo.14033193>.

Code availability

The code (ASPECT v2.3.0) used in this study is available in Bangerth et al.⁹¹.

Received: 7 April 2024; Accepted: 13 November 2024;

Published online: 02 December 2024

References

1. Stern, R. J. Subduction initiation: spontaneous and induced. *Earth Planet. Sci. Lett.* **226**, 275–292 (2004).
2. Arculus, R. J. et al. A record of spontaneous subduction initiation in the Izu–Bonin–Mariana Arc. *Nat. Geosci.* **8**, 728–733 (2015).
3. Stern, R. J. & Gerya, T. Subduction initiation in nature and models: a review. *Tectonophysics* **746**, 173–198 (2018).
4. Cramer, F. et al. A transdisciplinary and community-driven database to unravel subduction zone initiation. *Nat. Commun.* **11**, 1–14 (2020).
5. Gerya, T. V., Connolly, J. A. D. & Yuen, D. A. Why is terrestrial subduction one-sided? *Geology* **36**, 43–46 (2008).
6. Gerya, T. V., Stern, R. J., Baes, M., Sobolev, S. V. & Whattam, S. A. Plume-induced subduction initiation triggered plate tectonics on Earth. *Nature* **527**, 221–225 (2015).
7. Nikolaeva, K., Gerya, T. V. & Marques, F. O. Numerical analysis of subduction initiation risk along the Atlantic American passive margins. *Geology* **39**, 463–466 (2011).
8. Cooper, P. A. & Taylor, B. Polarity reversal in the solomon islands arc. *Nature* **314**, 428–430 (1985).
9. Tetreault, J. L. & Buiter, S. J. H. Geodynamic models of terrane accretion: testing the fate of island arcs, oceanic plateaus, and continental fragments in subduction zones. *J. Geophys. Res.* **117**, B08403–B08425 (2012).
10. Zhong, X. & Li, Z.-H. Subduction initiation during collision-induced subduction transference: Numerical modeling and implications for the Tethyan evolution. *J. Geophys. Res. Solid Earth* **125**, 1–27 (2020).
11. Wan, B. et al. Cyclical one-way continental rupture-drift in the Tethyan evolution: subduction-driven plate tectonics. *Sci China Earth Sci.* **62**, 2005–2016 (2019).
12. Yan, Z., Chen, L., Xiong, X., Wan, B. & Xu, H. Oceanic plateau and subduction zone jump: two-dimensional thermomechanical modeling. *J. Geophys. Res. Solid Earth* **126**, e2021JB021855 (2021).
13. Zhu, D. C. et al. The Lhasa terrane: record of a microcontinent and its histories of drift and growth. *Earth Planet. Sci. Lett.* **301**, 241–255 (2011).
14. Yan, Z., Chen, L., Zuza, A. V. & Meng, Q. Successive accretions of future allochthonous terranes and multiple subduction zone jumps: implications for Tethyan evolution. *Geol. Soc. Am. Bull.* **136**, 3230–3242 (2024).
15. Cui, F. Y. & Li, Z. H. Terrane collision-induced subduction initiation: mode selection and implications for western Pacific subduction system. *Geochem. Geophys. Geosyst.* **25**, e2023GC011155 (2024).
16. Whattam, S. A. & Stern, R. J. The ‘subduction initiation rule’: a key for linking ophiolites, intra-oceanic forearcs, and subduction initiation. *Contrib. Mineral. Petrol.* **162**, 1031–1045 (2011).
17. van Hinsbergen, D. J. J. et al. Dynamics of intraoceanic subduction initiation: 2. Suprasubduction zone ophiolite formation and metamorphic sole exhumation in context of absolute plate motions. *Geochem. Geophys. Geosyst.* **16**, 1771–1785 (2015).
18. Stern, R. J., Reagan, M., Ishizuka, O., Ohara, Y. & Whattam, S. To understand subduction initiation, study forearc crust: to understand forearc crust, study ophiolites. *Lithosphere* **4**, 469–483 (2012).
19. Zhou, X. et al. Subduction initiation dynamics along a transform fault control trench curvature and ophiolite ages. *Geology* **46**, 607–610 (2018).
20. Guilmette, C. et al. Forced subduction initiation recorded in the sole and crust of the Semail Ophiolite of Oman. *Nat. Geosci.* **11**, 688–695 (2018).
21. van Hinsbergen, D. J. J. et al. A record of plume-induced plate rotation triggering seafloor spreading and subduction initiation. *Nat. Geosci.* **14**, 626–630 (2021).
22. Windley, B. F., Alexelev, D., Xiao, W. J., Kroner, A. & Badarch, G. Tectonic models for accretion of the central Asian orogenic belt. *J. Geol. Soc., London* **164**, 31–47 (2007).
23. Xiao, W. J. et al. A tale of amalgamation of three Permo-Triassic collage systems in Central Asia: oroclines, sutures, and terminal accretion. *Annu. Rev. Earth Planet. Sci.* **43**, 477–507 (2015).
24. Zhu, M. S. et al. Discovery of a >1,000 km Cambrian eclogite-bearing high-pressure metamorphic belt in the Central Asian Orogenic Belt: implications for the final closure of the Pan-Rodinian Ocean. *J. Geophys. Res. Solid Earth* **128**, 1–28 (2023).
25. Wilhem, C., Windley, B. F. & Stampfli, G. M. The Altaiids of Central Asia: a tectonic and evolutionary innovative review. *Earth Sci. Rev.* **113**, 303–341 (2012).
26. Buriánek, D. et al. Geochemical and geochronological constraints on distinct early–Neoproterozoic and Cambrian accretionary events along southern margin of the Baydrag Continent in western Mongolia. *Gondwana Res.* **47**, 200–227 (2017).
27. Khain, E. V. et al. The most ancient ophiolite of the Central Asian fold belt: U–Pb and Pb–Pb zircon ages for the Dunzhugur Complex, Eastern Sayan, Siberia, and geodynamic implications. *Earth Planet. Sci. Lett.* **199**, 311–325 (2002).
28. Gordienko, I. V. et al. The late Riphean–Paleozoic history of the Uda–Vitim island arc system in the Transbaikalian sector of the Paleoasian ocean. *Russ. Geol. Geophys.* **51**, 461–481 (2010).
29. Štípká, P. et al. Early Cambrian eclogites in SW Mongolia: evidence that the Palaeo–Asian Ocean suture extends further east than expected. *J. Metamorph. Geol.* **28**, 915–933 (2010).
30. Skuzovatov, S. Y., Shatsky, V. S., Dril, S. I. & Perepelov, A. B. Elemental and isotopic (Nd–Sr–O) geochemistry of eclogites from the Zamyn–Nuruu area (SW Mongolia): crustal contribution and relation to Neoproterozoic subduction-accretion events. *J. Asian Earth Sci.* **167**, 33–51 (2018).
31. Li, Z. X. et al. Assembly, configuration, and break-up history of Rodinia: a synthesis. *Precambrian Res.* **160**, 179–210 (2008).
32. Zhao, G. C. et al. Geological reconstructions of the East Asian blocks: from the breakup of Rodinia to the assembly of Pangea. *Earth-Sci. Rev.* **186**, 262–286 (2018).
33. Jian, P. et al. Zircon dating of Neoproterozoic and Cambrian ophiolites in West Mongolia and implications for the timing of orogenic processes in the central part of the Central Asian Orogenic Belt. *Earth-Sci. Rev.* **133**, 62–93 (2014).
34. Ren, R. et al. When did the subduction first initiate in the southern Paleo-Asian Ocean: new constraints from a Cambrian intra-oceanic

- arc system in West Junggar, NW China. *Earth Planet. Sci. Lett.* **388**, 222–236 (2014).
35. Degtyarev, K. E., Luchitskaya, M. V., Tretyakov, A. A., Pilitsyna, A. V. & Yakubchuk, A. S. Early Paleozoic suprasubduction complexes of the North Balkhash ophiolite zone (Central Kazakhstan): geochronology, geochemistry and implications for tectonic evolution of the Junggar–Balkhash Ocean. *Lithos* **380**, 105818 (2021).
36. Yang, G. X., Li, Y. J., Tong, L. L., Wang, Z. P. & Si, G. H. An early Cambrian plume-induced subduction initiation event within the Junggar Ocean: insights from ophiolitic mélanges, arc magmatism, and metamorphic rocks. *Gondwana Res.* **88**, 45–66 (2020).
37. Badarch, G., Cunningham, D. W. & Windley, B. F. A new terrane subdivision for Mongolia: implications for the Phanerozoic crustal growth of Central Asia. *J. Asian Earth Sci.* **21**, 87–110 (2002).
38. Khukhuudei, U., Kusky, T., Windley, B. F., Otgonbayar, O. & Wang, L. Ophiolites and ocean plate stratigraphy (OPS) preserved across the Central Mongolian Microcontinent: a new mega-archive of data for the tectonic evolution of the Paleo-Asian Ocean. *Gondwana Res.* **105**, 51–83 (2022).
39. Soejono, I. et al. Early Palaeozoic sedimentary record and provenance of flysch sequences in the Hovd Zone (western Mongolia): implications for the geodynamic evolution of the Altai accretionary wedge system. *Gondwana Res.* **64**, 163–183 (2018).
40. Jiang, Y. D. et al. Neoproterozoic–early Paleozoic peri-Pacific accretionary evolution of the Mongolian collage system: insights from geochemical and U–Pb zircon data from the Ordovician sedimentary wedge in the Mongolian Altai. *Tectonics* **36**, 2305–2331 (2017).
41. Rubatto, D. Zircon trace element geochemistry: partitioning with garnet and the link between U–Pb ages and metamorphism. *Chem. Geol.* **184**, 123–138 (2002).
42. Jamyandorj, U., Tungalag, F. & Boishenko, A. F. *Geological Map of the Central and Eastern Mongolia, Scale 1:500000* (Ministry of Heavy Industrial (in Mongolia), 1990).
43. Sun, S. S. & McDonough, W. F. Chemical and isotopic systematics of oceanic basalts; implications for mantle composition and processes. *Geol. Soc. Spec. Publ.* **42**, 313–345 (1989).
44. Reagan, M. K. et al. Fore-arc basalts and subduction initiation in the Izu–Bonin–Mariana system. *Geochem. Geophys. Geosyst.* **11**, 1–17 (2010).
45. Hickey-Vargas, R. et al. Origin of depleted basalts during subduction initiation: evidence from IODP Expedition 351 Site U1438, Amami Sankaku Basin. *Geochim. Cosmochim. Acta* **229**, 85–111 (2018).
46. Stern, R. J. Subduction zones. *Rev. Geophys.* **40**, 1012 (2002).
47. Ishizuka, O., Tani, K. & Reagan, M. K. Izu–Bonin–Mariana forearc crust as a modern ophiolite analogue. *Elements* **10**, 115–120 (2014).
48. Kamei, A., Owada, M., Nagao, T. & Shiraki, K. High-Mg diorites derived from sanukitic HMA magmas, Kyushu Island, southwest Japan arc: evidence from clinopyroxene and whole rock compositions. *Lithos* **75**, 359–371 (2004).
49. Smithies, R. H. & Champion, D. C. The archaean high-Mg diorite suite: links to tonalite–trondhjemite–granodiorite magmatism and implications for Early Archaean crustal growth. *J. Petrol.* **41**, 1653–1671 (2000).
50. Macpherson, C. G. & Hall, R. Tectonic setting of Eocene boninite magmatism in the Izu–Bonin–Mariana forearc. *Earth Planet. Sci. Lett.* **186**, 215–230 (2001).
51. Tatsumi, Y. Geochemical modeling of partial melting of subducting sediments and subsequent melt–mantle interaction: generation of high-Mg andesites in the Setouchi volcanic belt, Southwest Japan. *Geology* **29**, 323–326 (2001).
52. Zeng, Y., Chen, J., Xu, J., Wang, B. & Huang, F. Sediment melting during subduction initiation: geochronological and geochemical evidence from the Darutso high-Mg andesites within ophiolite melange, central Tibet. *Geochem. Geophys. Geosyst.* **17**, 4859–4877 (2016).
53. Dilek, Y. & Furnes, H. Ophiolite genesis and global tectonics: geochemical and tectonic fingerprinting of ancient oceanic lithosphere. *Geol. Soc. Am. Bull.* **123**, 387–411 (2011).
54. Dick, H. J. B. & Bullen, T. Chromian spinel as a petrogenetic indicator in abyssal and alpine-type peridotites and spatially associated lavas. *Contrib. Miner. Petrol.* **86**, 54–76 (1984).
55. Ishizuka, O. et al. The time scales of subduction initiation and subsequent evolution of an oceanic island arc. *Earth Planet. Sci. Lett.* **306**, 229–240 (2011).
56. Yang, G. X. et al. Natural observations of subduction initiation: implications for the geodynamic evolution of the Paleo-Asian Ocean. *Geosyst. Geoenviron.* **1**, 100009 (2022).
57. Kröner, A. et al. Zircon and muscovite ages, geochemistry, and Nd–Hf isotopes for the Aktuyuz metamorphic terrane: evidence for an early Ordovician collisional belt in the northern Tianshan of Kyrgyzstan. *Gondwana Res.* **21**, 901–927 (2012).
58. Yang, Y. Q., Zhao, L., Zheng, R. G. & Xu, Q. Q. Evolution of the early Paleozoic Hongguleng–Balkybey Ocean: evidence from the Hebuskesaier ophiolitic mélange in the northern West Junggar, NW China. *Lithos* **324–325**, 519–536 (2018).
59. Jian, P., Liu, D., Shi, Y. & Zhang, F. SHRIMP dating of SSZ ophiolites from northern Xinjiang Province, China: implications for generation of oceanic crust in the Central Asian Orogenic belt. In, *Structural and Tectonic Correlation across the Central Asia Orogenic Collage: North-Eastern Segment Guidebook* (ed. Sklyarov, E.V.) 246 (2005).
60. Ao, S. J. et al. Cambrian to early silurian ophiolite and accretionary processes in the beishan collage, nw china: implications for the architecture of the southern altaids. *Geol. Mag.* **149**, 606–625 (2012).
61. Shi, Y. R., Zhang, W., Kröner, A., Li, L. L. & Jian, P. Cambrian ophiolite complexes in the Beishan area, China, southern margin of the Central Asian Orogenic Belt. *J. Asian Earth Sci.* **153**, 193–205 (2018).
62. Yang, Z. Y. et al. Early Cambrian oceanic crust in the Chinese North Tianshan: evidence of the earliest subduction system within the southwestern Central Asian Orogenic Belt. *Gondwana Res.* **119**, 104–118 (2023).
63. Zhu, M. S. et al. Zircon ages and geochemical compositions of the Manlay ophiolite and coeval island arc: Implications for the tectonic evolution of South Mongolia. *J. Asian Earth Sci.* **96**, 108–122 (2014).
64. Zhu, M. S. et al. Early Paleozoic oceanic inliers and reconstruction of accretionary tectonics in the Middle Gobi region, Mongolia: evidence from SHRIMP zircon U–Pb dating and geochemistry. *J. Asian Earth Sci.* **127**, 300–313 (2016).
65. Jian, P. et al. Time scale of an early to mid-Paleozoic orogenic cycle of the long-lived Central Asian Orogenic Belt, Inner Mongolia of China: implications for continental growth. *Lithos* **101**, 233–259 (2008).
66. Ding, P. Q. et al. Supra-subduction zone ophiolite generated by the initial subduction of an early Paleozoic island arc system abutting the northern North China Craton: evidence from meta-igneous rocks. *Gondwana Res.* **110**, 90–106 (2022).
67. Luo, Q. et al. Construction of an Early Cambrian intra-oceanic arc within the West Junggar, NW China: magmatic records from proto to mature-arc. *Lithos* **458–459**, 107343 (2023).
68. Safonova, I., Kotlyarov, A., Krivonogov, S. & Xiao, W. J. Intra-oceanic arcs of the Paleo-Asian Ocean. *Gondwana Res.* **50**, 167–194 (2017).
69. Shen, P., Pan, H., Seitmuratova, E., Yuan, F. & Jakupova, S. A. Cambrian intra-oceanic subduction system in the Bozshakol area, Kazakhstan. *Lithos* **224–225**, 61–77 (2015).
70. Degtyarev, K. E. Tectonic evolution of early Paleozoic island arc systems and continental crust formation in the Caledonides of Kazakhstan and the North Tien Shan. *Geotectonics* **45**, 23–50 (2011).

71. Xu, X. Y. et al. Geochemistry and geochronology of Paleozoic intrusions in the Nalati (Narati) area in western Tianshan, Xinjiang, China: implications for Paleozoic tectonic evolution. *J. Asian Earth Sci.* **72**, 33–62 (2013).
72. Li, M. et al. Composition, age and P polarity of Gongpoquan arc and its tectonic significance in Beishan Orogen. *Earth Sci.* **7**, 2393–2412 (2020).
73. Soejono, I. et al. A reworked Lake Zone margin: chronological and geochemical constraints from the Ordovician arc-related basement of the Hovd Zone (western Mongolia). *Lithos* **295**, 112–132 (2017).
74. Demoux, A., Kröner, A., Liu, D. & Badarch, G. Precambrian crystalline basement in southern Mongolia as revealed by SHRIMP zircon dating. *Int. J. Earth Sci.* **98**, 1365–1380 (2009).
75. Zhang, S. H., Zhao, Y., Ye, H., Liu, J. M. & Hu, Z. C. Origin and evolution of the Bainaimiao arc belt: implications for crustal growth in the southern central Asian orogenic belt. *Geol. Soc. Am. Bull.* **126**, 1275–1300 (2014).
76. Zhou, H., Zhao, G. C., Han, Y. G. & Wang, B. Geochemistry and zircon U-Pb-Hf isotopes of paleozoic intrusive rocks in the damao area in Inner Mongolia, northern China: implications for the tectonic evolution of the bainaimiao arc. *Lithos* **314**, 119–139 (2018).
77. Zhou, J. B. et al. A > 1300 km late Pan-African metamorphic belt in NE China: new evidence from the Xing'an Block and its tectonic implications. *Tectonophysics* **509**, 280–292 (2011).
78. Yang, Y. et al. Metamorphic evolution of high-grade granulite-facies rocks of the Mashan Complex, Liumao area, eastern Heilongjiang Province, China: evidence from zircon U-Pb geochronology, geochemistry and phase equilibria modelling. *Precambrian Res.* **355**, 106095 (2021).
79. Gladkochub, D. P. et al. Petrology, geochronology, and tectonic implications of c. 500 Ma metamorphic and igneous rocks along the northern margin of the Central Asian Orogen (Olkhon terrane, Lake Baikal, Siberia). *J. Geol. Soc.* **165**, 235–246 (2008).
80. Wang, X. S. et al. Final assembly of the southwestern central Asian orogenic belt as constrained by the evolution of the south Tianshan orogen: links with Gondwana and Pangea. *J. Geophys. Res., Solid Earth* **123**, 7361–7388 (2018).
81. Zhang, R. Y. et al. U-Pb geochronology of zircon and rutile from the Kokchetav metamorphic belt, northern Kazakhstan, and its tectonic implications. *Eur. J. Mineral.* **28**, 1203–1213 (2016).
82. Kravchinsky, V. A., Sklyarov, E. V., Gladkochub, D. B. & Harbert, W. P. Paleomagnetism of the Precambrian Eastern Sayan rocks: implications for the Ediacaran–early Cambrian paleogeography of the Tuva–Mongolian composite terrane. *Tectonophysics* **486**, 65–80 (2010).
83. Zhou, X., Li, Z. H., Gerya, T. V. & Stern, R. J. Lateral propagation-induced subduction initiation at passive continental margins controlled by preexisting lithospheric weakness. *Sci. Adv.* **6**, eaaz1048 (2020).
84. Hall, R. The subduction initiation stage of the wilson cycle. *Geol. Soc. London, Spec. Publ.* **470**, 415–437 (2019).
85. Cawood, P. A. et al. Gondwana's interlinked peripheral orogens. *Earth Planet. Sci. Lett.* **568**, 117057 (2021).
86. Cawood, P. A. & Buchan, C. Linking accretionary orogenesis with supercontinent assembly. *Earth-Sci. Rev.* **82**, 217–256 (2007).
87. Murphy, J. B., Pisarevsky, S. & Nance, R. D. Potential geodynamic relationships between the development of peripheral orogens along the northern margin of Gondwana and the amalgamation of West Gondwana. *Miner. Petrol.* **107**, 635–650 (2013).
88. Yao, J. et al. Mariana-type ophiolites constrain the establishment of modern plate tectonic regime during Gondwana assembly. *Nat. Commun.* **12**, 4189 (2021).
89. Shan, H. et al. Subduction initiation of the Proto-Tethys Ocean that facilitated climate change and biodiversification. *Earth Planet. Sci. Lett.* **600**, 117874 (2022).
90. Kronbichler, M., Heister, T. & Bangerth, W. High accuracy mantle convection simulation through modern numerical methods. *Geophys. J. Int.* **191**, 12–29 (2012).
91. Heister, T., Dannberg, J., Gassmäller, R. & Bangerth, W. High accuracy mantle convection simulation through modern numerical methods-II: realistic models and problem. *Geophys. J. Int.* **210**, 833–851 (2017).
92. Bangerth, W. et al. ASPECT v2.3.0 (v2.3.0). https://open.clemson.edu/all_data/506/ (2021).
93. Bercovici, D. & Mulyukova, E. Evolution and demise of passive margins through grain mixing and damage. *Proc. Natl. Acad. Sci. USA* **118**, e2011247118 (2021).
94. Toth, J. & Gurnis, M. Dynamics of subduction initiation at preexisting fault zones. *J. Geophys. Res.* **103**, 18053–18067 (1998).
95. Pearce, J. A., 2003, Supra-subduction zone ophiolites: the search for modern analogues. In *Ophiolite Concept and the Evolution of Geological Thought* (eds. Dilek, Y. & Newcomb, S.) 373 (Geological Society of America, 2003).
96. Stampfli, G. M. & Borel, G. D. A plate tectonic model for the Paleozoic and Mesozoic constrained by dynamic plate boundaries and restored synthetic oceanic isochrons. *Earth Planet. Sci. Lett.* **196**, 17–33 (2002).
97. Sun, W., Zhang, L., Li, H. & Liu, X. The synchronous Cenozoic subduction initiations in the west Pacific induced by the closure of the Neo-Tethys Ocean. *Sci. Bull.* **65**, 2068–2071 (2020).
98. Ludwig, K.R. Squid 1.03 A User's Manual. *Sci. Res.* **5**, 7 (2001).
99. Ludwig, K.R. *User's Manual for Isoplot 3.0*. <https://search.worldcat.org/> (2003).
100. Compston, W., Williams, I. S. & Mayer, C. U-Pb geochronology of zircons from Lunar Breccia 73217 using a sensitive high resolution ion microprobe: proc. XIV lunar planetary science conference. *J. Geophys. Res.* **89**, B525–B534 (1984).
101. Wu, F. Y., Yang, Y. H., Xie, L. W., Yang, J. H. & Xu, P. Hf isotopic compositions of the standard zircons and baddeleyites used in U-Pb geochronology. *Chem. Geol.* **234**, 105–126 (2006).
102. Griffin, W. L. et al. The Hf isotope composition of cratonic mantle: LAM-MC-ICPMS analysis of zircon megacrysts in kimberlites. *Geochim. Cosmochim. Ac.* **64**, 133–147 (2000).
103. Sláma, J. et al. Plešovice zircon—a new natural reference material for U-Pb and Hf isotopic microanalysis. *Chem. Geol.* **249**, 1–35 (2008).
104. Glerum, A. C., Thielot, C., Fraters, M., Blom, C. & Spakman, W. Nonlinear viscoplasticity in ASPECT: benchmarking and applications to subduction. *Solid Earth* **9**, 267–294 (2018).

Acknowledgements

We thank Robert J. Stern and five anonymous reviewers for their constructive comments and suggestions, and Carolina Ortiz Guerrero for editorial handling and helpful comments. We are grateful to Shuangrong Zhang and Hongfang Chen for their supports of the analytical experiments. We thank Munkhtsengel Baatar and Chimedtsuren Anaad for their supports during our field investigations in Mongolia. This work was financially supported by the National Natural Science Foundation of China (grant Nos. 42272262 and 42172241), Strategic Priority Research Program of Chinese Academy of Sciences (grant No. XDB 41000000), the Second Tibetan Plateau Scientific Expedition and Research Program (Grant No. 2019QZKK0806) and Ramón y Cajal Fellowship from the Spanish Ministry of Science and Innovation (Grant RYC2019-028244-I). This is also a contribution to the project of Theory of Hydrocarbon Enrichment under Multi-Spheric Interactions of the Earth (THEMSIE).

Author contributions

M.Z., D.P.G. and S.L. designed the project and wrote the original manuscript. M.A.S., L.M., F.Z., M.D. and A.G. prepared the revised manuscript. M.D. performed model simulations. M.Z., L.M. and D.S.

conducted the mapping and sampling. M.Z., C.L. and Y.L. finished all the analyses. All authors contributed to the interpretation of the results.

Competing interests

The authors declare no competing interests.

Additional information

Supplementary information The online version contains supplementary material available at
<https://doi.org/10.1038/s43247-024-01905-7>.

Correspondence and requests for materials should be addressed to Mingshuai Zhu, Miao Dong or Shun Li.

Peer review information *Communications Earth & Environment* thanks Karel Schulmann, Chenwei Li and the other, anonymous, reviewer(s) for their contribution to the peer review of this work. Primary Handling Editor: Carolina Ortiz Guerrero. A peer review file is available.

Reprints and permissions information is available at
<http://www.nature.com/reprints>

Publisher's note Springer Nature remains neutral with regard to jurisdictional claims in published maps and institutional affiliations.

Open Access This article is licensed under a Creative Commons Attribution-NonCommercial-NoDerivatives 4.0 International License, which permits any non-commercial use, sharing, distribution and reproduction in any medium or format, as long as you give appropriate credit to the original author(s) and the source, provide a link to the Creative Commons licence, and indicate if you modified the licensed material. You do not have permission under this licence to share adapted material derived from this article or parts of it. The images or other third party material in this article are included in the article's Creative Commons licence, unless indicated otherwise in a credit line to the material. If material is not included in the article's Creative Commons licence and your intended use is not permitted by statutory regulation or exceeds the permitted use, you will need to obtain permission directly from the copyright holder. To view a copy of this licence, visit <http://creativecommons.org/licenses/by-nc-nd/4.0/>.

© The Author(s) 2024